Check for updates

A mesoporous Mo and N Co-doped TiO$_2$ nanocomposite with enhanced photocatalytic efficiency

Ayman K. El-Sawaf,[ab] Amal A. Nassar,[a] Dina A. Tolan,*[ab] Mohamed Ismael,[c] Islam Alhindawy, [c] Ekramy M. El-Desouky,[c] Ahmed El-Nahas, [b] Mohammed Shahien[d] and Mai Maize [b]

This study reports the synthesis of a mesoporous Mo and N codoped anatase TiO$_2$ nanocomposite with many oxygen vacancies using a simple one-step hydrothermal method and subsequent calcination treatment. Both Mo and N were effectively co-incorporated into the anatase phase of TiO$_2$ without MoO$_x$ phase segregation. The codoped catalyst demonstrated a mesoporous architecture with a surface area of 107.48 m^2 g^{-1} and a pore volume of 0.2974 cm^3 g^{-1}. X-ray photoelectron spectroscopy confirmed that both Mo and N dissolved in the TiO$_2$ lattice and created induced oxygen vacancies. The interaction of the dopants (Mo and N) and oxygen vacancies clearly affected TiO$_2$ crystal formation. Photocatalytic performance of the nanocomposite was investigated in terms of the decomposition of methyl orange at a concentration of 50 mg L^{-1} in an aqueous solution. The results revealed a significant methyl orange degradation of up to 99.6% after 30 min irradiation under a UV light. The impressive performance of the nanocomposite is assigned to the synergetic effect of important factors, including the co-doping of metallic (Mo) and non-metallic (N) elements, oxygen vacancy defects, bandgap, crystallite size, mesoporous structure, and BET surface area.

1. Introduction

Fabrication of nanostructured semiconductors is gaining considerable attention owing to their ability to absorb solar light radiation and their promising implications in environmental remediation *via* photocatalytic redox reactions.[1–5] Currently, titanium dioxide (TiO$_2$) has been popularly utilized as a photocatalyst for the degradation of pollutants and energy conversion owing to its excellent advantages, including high refractive index, superior photocatalytic efficiency, low cost, high thermal and chemical stability, and non-toxicity.[6–9] However, the wide bandgap (3.2 eV for anatase) of TiO$_2$ can only be activated using ultraviolet (UV) light, which has limited its practical applicability in visible-light-driven chemical reactions[10,11] in addition to the fast recombination rate of photogenerated charge carriers.[10,11] .

Therefore, considerable efforts have been devoted toward widening the utilization scope of TiO$_2$ not only *via* extending the

photosensitivity of TiO$_2$ to the visible light region but also by diminishing the recombination rate of charge carriers.[4,7,11] Doping or codoping TiO$_2$ with heteroatoms (metals or/and non-metals) is a promising strategy for narrowing its bandgap and thereby increasing the photocatalytic performance.[4,7,11] Nitrogen is the most promising anionic dopant for TiO$_2$ because the size and ionization energy of both nitrogen and oxygen are almost identical.[12,13] Moreover, nitrogen narrows the TiO$_2$ bandgap *via* coupling its 2p states with the 2p states those of TiO$_2$ oxygen, thus forming electronic levels above the valence band of O 2p.[10,12,13] Note that doping TiO$_2$ with a metal having a higher oxidation state (especially Molybdenum; Mo^{6+}) than that of the parental Ti^{4+} atom would increase the separation and transfer of the photogenerated charge carriers.[14] Molybdenum has a partially filled d electron shell and a tunable valence state, which make it a good doping candidate for fine-tuning the catalytic efficiency of a material.[15,16] Furthermore, Mo is widely used as a TiO$_2$ dopant as it is non-toxic and inexpensive with good solubility in the anatase phase.[14] Moreover, the similar radii of Mo^{6+} ions (0.062 nm) and Ti^{4+} ions (0.068 nm) facilitate effective Mo^{6+} substitution at Ti^{4+} sites with minimal or no lattice distortion.[14,17–22] As for charge balancing, the Mo^{5+} species is usually produced (though Mo^{6+} is used as the doping precursor); otherwise, Ti^{3+} species or/and oxygen vacancies are formed.[23] Oxygen vacancies are the most popular type of TiO$_2$ intrinsic defects and are assumed to be the most active regions

aDepartment of Chemistry, College of Science and Humanities, Prince Sattam bin Abdulaziz University, Alkharj 11942, Saudi Arabia. E-mail: d.tolan@psau.edu.sa

bDepartment of Chemistry, Faculty of Science, Menoufia University, Shibin El-Kom, Egypt

cNuclear Materials Authority, El Maadi, Cairo, Egypt

dCentral Metallurgical Research & Development Institute (CMRDI), Helwan 11421, Egypt

in TiO_2.[13] The presence of both oxygen-deficient regions and intrinsic Ti^{3+} surface defects induce the formation of new mid-bandgap levels that are located below the conduction band and act as donor or acceptor electronic levels.[13,14]

Though mono-doping can diminish the TiO_2 bandgap to some extent, it suffers from the presence of recombination centers and the creation of tightly localized impurity bands inside the bandgap, which reduce carrier mobility.[17,22] Thus, co-doping with a metal-cation and a nonmetal-anion has been reported to minimize the recombination centers *via* passivating the defect bands and preventing them from serving as recombination centers.[4,17,24] Many studies demonstrated the remarkable enhancement of TiO_2 photoactivity *via* Mo and N co-doping and the shift in its light absorption ability to the visible light range.[17,18,22,24,25] However, the development of a facile approach to fabricate nanostructured semiconductor photocatalysts with visible-light photocatalytic efficiency remains a challenge.

This study aims to promote the photoresponse of anatase titania to visible light and thereby its photocatalytic performance by a facile hydrothermal process that achieves Mo and N codoping and oxygen deficiency formation. The prepared nanocomposite was characterized for elucidating the noticeable improvement in photoactivity. The photocatalytic activity of the obtained nanocomposite was evaluated in the photo-degradation of methyl orange solution under UV light irradiation. Relevant reasons for its superior photocatalytic performance are outlined.

2. Experimental

2.1. Chemicals

The starting materials, including commercially available ammonium molybdate tetrahydrate (AMT: $(NH_4)_6Mo_7O_{24} \cdot 4H_2O$; 99.9%), ammonium oxalate ($C_2H_8N_2O_4$; 99.5%), ascorbic acid ($HC_6H_7O_6$; 99%), titanium(III) chloride ($TiCl_3$; 99%), sodium lauryl sulfate (SLS: $NaC_{12}H_{25}SO_4$; 99%), ethanol (C_2H_5OH; 99.9%) and methyl orange ($C_{14}H_{14}N_3NaO_3S$; 85%), were obtained from Sigma-Aldrich (Missouri, United States). Double distilled water (DIW) was used for sample preparation.

2.2. Photocatalyst preparation

Porous (Mo + N) codoped TiO_2 nanocomposite powders with carbon-modified surfaces were synthesized using a hydrothermal process. A mixture of 0.1 g AMT, 0.5 g ammonium oxalate, and 0.5 g ascorbic acid was homogeneously blended in a manual mill. The mixture was dropped into a solution of 15 mL titanium(III) chloride, 0.2 g SLS, and 75 mL DIW and vigorously stirred for 45 min until a gel was formed. The fabricated gel was transferred to a Teflon-lined stainless steel autoclave (100 mL), sealed, and maintained in an oven at 155 °C for 40 h. The autoclave was then naturally cooled to room temperature in the air. The obtained precipitates were filtered, washed with DIW and ethanol several times and dried at 65 °C for 5 h under a vacuum. Finally, the fabricated samples were calcined at 500 °C for 3 h in the air by heating at a rate of 2° C min⁻¹. The final product was defined as a Mo-doped TiO_2

photocatalyst (MT1). Similar procedures were repeated by varying the content of ammonium molybdate tetrahydrate to 0.2 and 0.3 g for fabricating catalysts with different Mo doping amounts, and these are defined as MT2 and MT3, respectively. Furthermore, undoped TiO_2 was prepared by the same method without adding the Mo precursor and used as a reference.

2.3. Characterizations of the synthesized photocatalyst

The phase structure of synthesized powders was identified using an X-ray diffractometer (XRD, Panalytical X'Pert Pro) with CuKα radiation (wavelength of 0.15406 nm) operated at 45 kV, 40 mA, and 25 °C. The spectra were recorded in the range of 10°–80° with a step size of 0.013. The surface microstructure and elemental composition were observed using a scanning electron microscope (SEM, JEOL JSM, Japan) equipped with an energy-dispersive X-ray (EDX) detector. The N_2 adsorption–desorption isotherm measurement was conducted at 77 K using the ChemBET Pulsar TPR/TPD instrument. X-ray photoelectron spectroscopy (XPS) was performed using equipment from ThermoFisher Scientific, USA system (USA) to investigate the surface chemical composition. The elemental analysis was performed using inductively coupled plasma-optical emission spectrometry (ICP-OES, LabTech, USA). EIS measurements of both un-doped and doped titanium oxide were conducted by applying an AC signal with a 10 mV amplitude in the frequency range of 0.1 Hz–50 M Hz at the open-circuit potential.

2.4. Photocatalytic activity

The photocatalytic efficiency of the as-prepared samples was evaluated using a Hitachi U-3900H double-beam UV-visible spectrophotometer in the region of 250–750 nm. The photocatalytic activity of the samples was estimated in terms of methyl orange dye (MO, a model pollutant) degradation under UV-Vis light illumination (wavelength range: 200 to 900 nm) using a 350 nm UV lamp. The MO photodegradation experiments were performed in the air at room temperature inside a sealed and black-painted wooden box with a UV lamp installed on the top. The degradation test was performed using the batch method under continuous stirring using a magnetic stirrer. In a typical run, 10 mg of the synthesized photocatalyst powder was added to a beaker containing 10 mL of MO solution at 50 mg L⁻¹. The mixture was sonicated under UV light for an appropriate time, and the reaction mixtures were collected at regular intervals by instant filtration. The decolorization of the dye solution was determined by measuring its absorbance at 460 nm on a UV-visible spectrophotometer as a function of exposure time.

3. Results and discussion

3.1. Crystal phase analysis of the synthesized photocatalysts

Herein, we present the analysis of only one of the doped TiO_2 samples, namely MT3, as it exhibited the best photocatalytic activity compared with other samples. The ICP analysis confirmed that the Mo concentration per gram of TiO_2 was 83 mg (8.3 wt%). The phase spectrum of the synthesized Mo–N
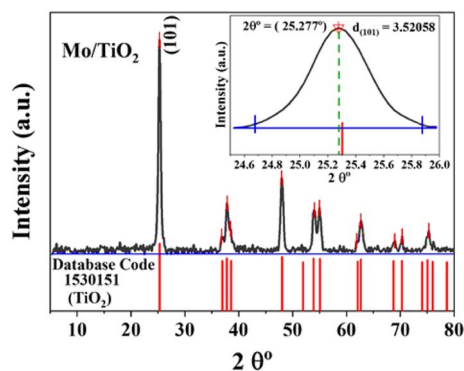
Fig. 1 The XRD pattern of the as-prepared (Mo + N) codoped TiO$_2$ NPs.

codoped TiO$_2$ powder is shown in Fig. 1. All the identified peaks perfectly refer to the anatase phase only (database code no: 1530151), which reveals a highly crystalline structure.[21,26] The high crystallinity is beneficial to increasing the photocatalytic efficiency of the powder. The characteristic peaks at the approximate 2θ values of 25.227° (101), 37.827° (004), 38.477° (200), 54.027° (105), 54.977° (211), 62.677° (204), 68.977° (116), 70.327° (220) and 75.277° (215) correspond to the anatase phase (database code: 1530151).[21,26] Remarkably, the diffraction pattern of the doped TiO$_2$ sample was fairly identical to pure TiO$_2$ (database code: 1530151) but with a slight shift in peak positions, as shown in the inset of Fig. 1. Moreover, no significant peaks of the free Mo phases were detected. This indicates that the Mo^{6+} ions were incorporated into the TiO$_2$ crystal lattice by either substituting the Ti^{4+} ions or occupying vacant sites in the lattice.[22,27,28] Since the radii of the Mo^{6+} ions (0.062 nm) and Ti^{4+} ions (0.068 nm) are very similar, Mo can easily substitute Ti^{4+} and occupy its lattice position rather than an interstitial position. This leads to changes in the crystal plane distance and lattice parameters (lattice contraction), as previously reported.[14,17–20] Note that Mo incorporation might not be detected by XRD as it could be below the detection limit, as reported previously.[20] The changing color of TiO$_2$ with the Mo content confirmed Mo incorporation. Lattice distortion owing to the dopants (ε) was calculated based on the following formula,[29,30] $\varepsilon = \beta/(4 \tan \theta)$, where β is the full width at half maximum (FWHM) of the main peak and θ is the reflection angle. The Mo–N codoped TiO$_2$ composite revealed a lattice distortion of 0.3595, which may lead to an increase in lattice defects and assist carrier recombination.[28,31] Moreover, (101) was the dominant plane, which signifies that the Mo–N codoped TiO$_2$ photocatalyst would preferably exhibit a (101) aligned texture. The d-spacings or interplanar spacings between the lattice fringes (d_{hkl}) were calculated from X-ray diffraction data using the Bragg Equation $d = (n \lambda)/(2 \sin \theta)$,[32] where d indicates the distance between the atomic layers, λ is the wavelength of the incident X-ray beam, and n is an integer = 1. All d_{hkl} of Mo–N codoped TiO$_2$ matched well with those of TiO$_2$ in the database code, except for d_{101}, which was 3.52058 nm. This fluctuation in lattice characteristics might reflect a change in oxygen

vacancies, which are often related to the incorporation of impurities.[33] The average crystallite size (D) was evaluated by the Scherrer formula $D = (K \lambda)/(\beta \cos \theta)$,[34] where K is the shape factor (here 0.89), λ is the X-ray radiation wavelength (0.15406 nm for Cu Kα), θ is the reflection angle and β is the FWHM. Mo–N codoped TiO$_2$ exhibited a crystallite size of 18.144 nm. Using the full width at half maximum (FWHM) of the (101) diffraction peak, the (101) interplanar distance in Mo–N codoped TiO$_2$ was found to be 0.352 nm, which is somewhat greater than that of pure TiO$_2$ anatase (0.35165 nm), indicating that the N and Mo atoms were implanted in the TiO$_2$ lattice.[17]

3.2. Morphological analysis of the as-synthesized photocatalysts

Fig. 2 shows the surface morphology and EDX elemental mappings of the as-prepared photocatalysts. The SEM images in Fig. 2(a and b) reveal that the as-prepared nanocomposite had a pseudo-spherical morphology with numerous caves and mounds. This can be attributed to the slight agglomeration of the nanocrystals. The elemental mappings of the Mo and N codoped TiO$_2$ NPs in Fig. 2 (c–f) indicate the uniform distribution of Ti, O, and Mo in the as-prepared composites. The EDX elemental spectrum in Fig. 2(g) indicates that the as-prepared photocatalyst NPs comprised Ti, O, and Mo without any impurities, and the Mo-doping content was 3.93 atomic%. The N peak was not particularly noticeable probably because of the low N content in TiO$_2$.[22,35]

3.3. Textural properties of the as-synthesized photocatalysts

The surface area, type of adsorption isotherms, and the pore sizes/shapes are important factors that determine the catalytic performance. Therefore, the textural features of the as-prepared Mo and N codoped TiO$_2$ NPs were investigated using the N$_2$ sorption technique at a low temperature of 77 K. The nitrogen desorption results, as shown in Fig. 3(a), demonstrated a typical type IV isotherm with a type H3 hysteresis loop, indicating the formation of a mesoporous structure with slit-shaped pores as a result of the stacking of plate-like particles.[36,37] Furthermore, the corresponding pore size distribution was calculated using the Barrett–Joyner–Halenda (BJH) method from the desorption branch of the isotherm, as shown in Fig. 3(b). The BET specific surface area (S_{BET}) was 107.48 m^2 g^{-1}, and the total pore volume was 0.2974 cm^3 g^{-1}. The measured values indicate that the as-prepared material has excellent surface and mesoporous properties and thereby will lead to high photocatalytic activity. Moreover, the incorporation of a dopant is coupled with the emergence of various defects in the TiO$_2$ crystal structure. The accumulation of defects, such as oxygen vacancies, assists the generation of pores, thus boosting the surface area, providing more active sites, and consequently enhancing the photocatalytic activity of the prepared photocatalyst.[11,38,39]

3.4. XPS analysis and electronic structure

The XPS analysis was used to explore the bonding interaction and the oxidation states of the constituent elements in undoped TiO$_2$ and the (Mo + N) codoped TiO$_2$ nanocomposite. Whenever
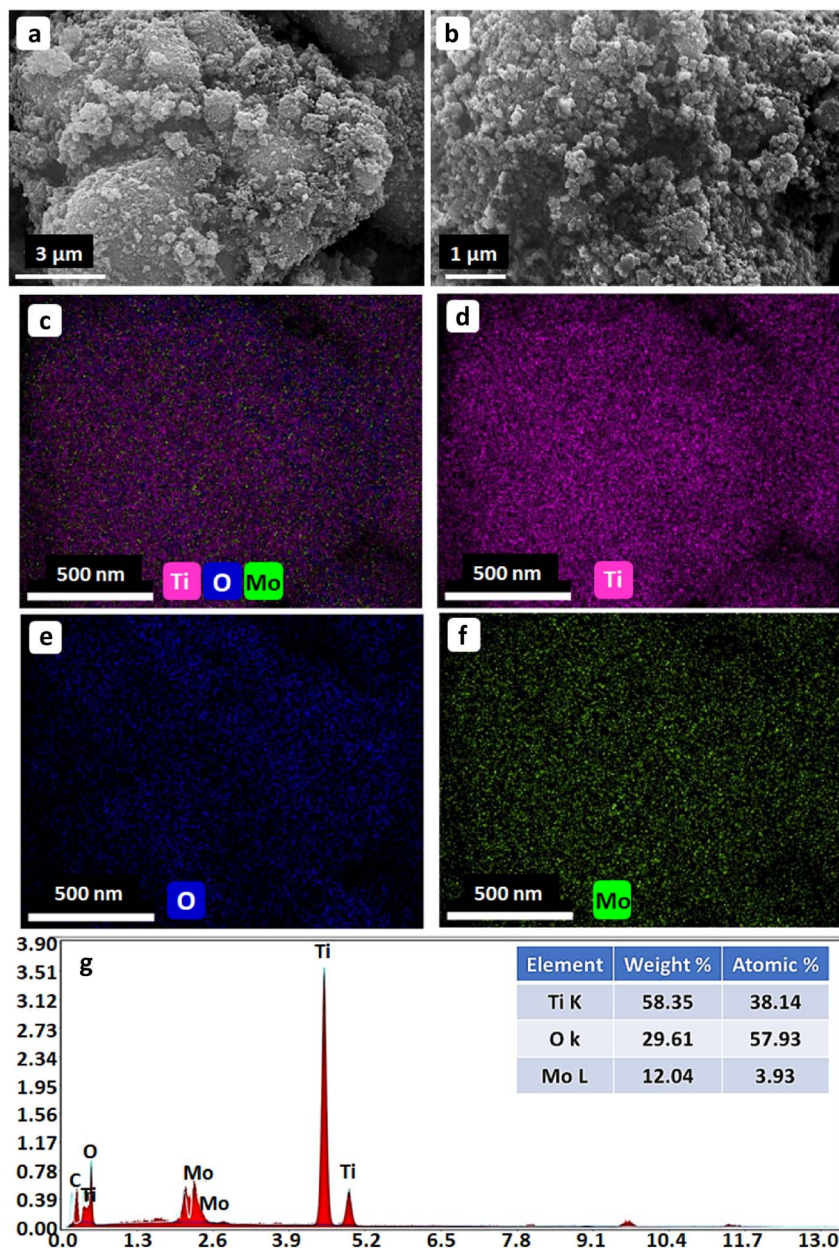
Fig. 2 The SEM images of the as-prepared (Mo + N) codoped TiO_2 NPs at (a) low magnification and (b) high magnification; (c–f) the EDX elemental mappings and (g) EDX spectrum of the as-prepared (Mo + N) codoped TiO_2 NPs.

isomorphic substitution takes place owing to the codoping of Mo and N, the extra positive charges offered by the Mo^{6+} species would be compensated using different means. This includes the creation of oxygen vacancies, the generation of (reduced) Mo^{6+} ions, and the reduction of Ti^{4+} ions to Ti^{3+} ions (intervalence charge transfer (IVCT)).[21,23,40] The XPS spectra of as-prepared nanocomposites clearly confirmed the existence of Ti, Mo, O, N, and C, as shown in Fig. 4(a), indicating the effective formation of the Mo and N codoped TiO_2 nanocomposite. The presence of C could be attributed to the contamination of adventitious carbon. The Mo content (atomic ratio) was 4.96%, which is higher than the theoretical value of 3.6%, revealing the surface enrichment of the Mo ions.[21,23,31] Furthermore, the

intensity and width of the N 1s peak of the doped sample were higher than those of bare TiO_2. This is presumably related to the crystal lattice distortion caused by Mo doping, which facilitates the doping and solubility of N atoms in the structure.[22,25]

Compared with undoped TiO_2, in Fig. 4(b), (Mo + N) codoping slightly reduces the binding energies of the $Ti2p_{1/2}$ and $Ti2p_{3/2}$ orbitals. This reveals a relative drop in Ti valence, that is, the conversion of Ti^{4+} ions to Ti^{3+} accompanied by oxygen loss (oxygen vacancies) from the TiO_2 surface and substitution with N and Mo.[40] Fig. 4(c) shows the high-resolution XPS scan over the Ti2p peak of the (Mo + N) codoped TiO_2 nanocomposite. It reveals two distinct peaks at about 464.17 and 458.43 eV, which are indexed to the $Ti2p_{1/2}$ and
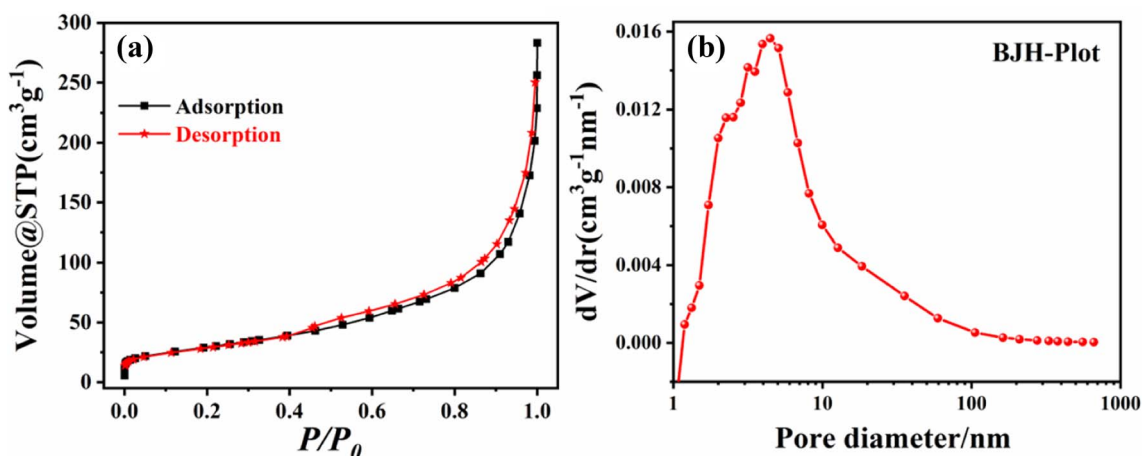
Fig. 3   (a) The N_2 adsorption–desorption isotherm and (b) BJH pore-size distribution (BJH plot) of the as-prepared (Mo + N) codoped TiO_2 NPs.

$Ti2p_{3/2}$ orbitals of Ti^{4+} (TiO_2), respectively.[41–43] Moreover, the split of the 5.7 eV peak between the Ti2p doublets clearly confirms the presence of Ti^{4+} ions in the TiO_2 lattice.[43–46] Furthermore, some peaks revealing the presence of the Ti^{3+} and Ti^{2+} oxidation states were observed.[47,48] The peaks at 463.16 and 457.93 eV are attributed to the $Ti2p_{1/2}$ and $Ti2p_{3/2}$ orbitals of Ti^{3+} present in the TiO_2 lattice,[47,48] which confirms the conversion of Ti^{4+} to Ti^{3+} upon Mo-doping *via* intervalence charge transfer (IVCT). In this process, a charge compensation mechanism occurs; the reduction of Ti^{4+} to the less stable Ti^{3+} ion is associated with Mo^{5+} oxidation to the more stable Mo^{6+} phase.[21,40] The difference in the redox potentials of Ti^{4+}/Ti^{3+} (0.1 eV) and Mo^{6+}/Mo^{5+} (0.4 eV) assists the capture of the electrons photogenerated by the Mo^{6+} ions. Consequently, the recombination rate of the e^-/h^+ pairs is reduced, leading to enhancement in the photocatalytic activity.[25,49]

$Mo3d_{5/2}$ and $Mo3d_{3/2}$ peaks with higher binding energy were observed at 232.43 and 235.53 eV, as shown in Fig. 4(d). These are attributed to the Mo^{6+} oxo-species with a 3.1 eV spin-orbital doublet splitting.[27,50] Furthermore, the signals at lower binding energies of 231.69 and 235 eV are ascribed to the $Mo3d_{5/2}$ and $Mo3d_{3/2}$ of Mo^{5+} oxo-species, respectively.[19,41,51,52] Therefore, the Mo^{6+} and Mo^{5+} states of Mo coexist at an atomic proportion of 71.4% and 28.6%, respectively. The presence of Mo^{5+} ions is a sign of oxygen deficiency.[19] The O 1s XPS spectrum could be deconvoluted into only two signals, as shown in Fig. 4(e). The higher signal centered at 529.68 eV corresponds with the oxygen within the TiO_2 crystal lattice ($Ti^{4+}–O$).[41,53] The lower energy signal at 530.05 eV is presumably attributed to the adsorbed oxygen in the oxygen-deficiency regions (owing to lattice distortion and the porous structure).[19,27,31,41] Herein, the as-prepared (Mo + N) codoped TiO_2 NPs exist in an oxygen-deficient state owing to the inclusion of the dopant cations. Thus, one Ti atom requires two O atoms, whereas one Mo atom requires three O atoms, as well as due to the presence of the Mo^{5+} ions.[19,53] Fig. 4(e) and its inset show the comparison between doped and undoped TiO_2. It reveals higher O adsorption on the surface of the (Mo + N) codoped TiO_2

nanocomposite compared with the bare TiO_2 surface. The lack of oxygen on the surface can be complemented by adsorbing more oxygen, which is considered an advantage for photocatalytic degradation.[19,41] Furthermore, the N 1s peak was located at 399.5 eV (Fig. 4(f)), suggesting that the nitrogen atoms were interstitially incorporated in the TiO_2 lattice and formed Ti–N–O or Ti–O–N oxynitride linkages.[24,54–57] This observation reveals that metal doping enhances N solubility in the TiO_2 lattice.[22] Moreover, the existence of the N dopant is accompanied by the creation of oxygen vacancies.[58]

The estimated oxidation-reduction potentials of Ti^{4+}/Ti^{3+} and Mo^{6+}/Mo^{5+} are 0.1 and 0.4 eV[25], respectively. This indicates the greater ability of Mo^{6+} to catch photogenerated electrons, get distinct carriers, and boost the photocatalytic efficiency. Therefore, the photogenerated electrons can be captured, the rate of electron–hole recombination can be minimized and the photocatalytic reaction can be accelerated by injecting a suitable amount of the dopants.[25]

3.5.   Electrochemical impedance spectroscopy (EIS)

EIS is a powerful technique used to probe the various kinetic processes occurring at the electrode–electrolyte interface. Electrochemical impedance spectroscopy across a wide frequency range was conducted to extensively understand the electrode kinetics. The Nyquist plots (Fig. 5) of both undoped TiO_2 and Mo-doped TiO_2 samples displayed characteristic signatures of charge transfer and ion diffusion processes. Note that the diameter of the semicircular arc was smaller for Mo–TiO_2, indicating faster charge transfer kinetics compared to pure TiO_2. This enhancement arises from the oxygen vacancies introduced in the material when the Ti^{4+} ions are partially substituted by Mo^{6+} during doping.[59,60] The oxygen vacancies compensate for the charge imbalance and dramatically increase the electrical conductivity. By providing additional pathways for charge transport, the oxygen vacancies facilitate faster charge transfer across the Mo–TiO_2 sample, thereby reducing the cumulative internal resistance.
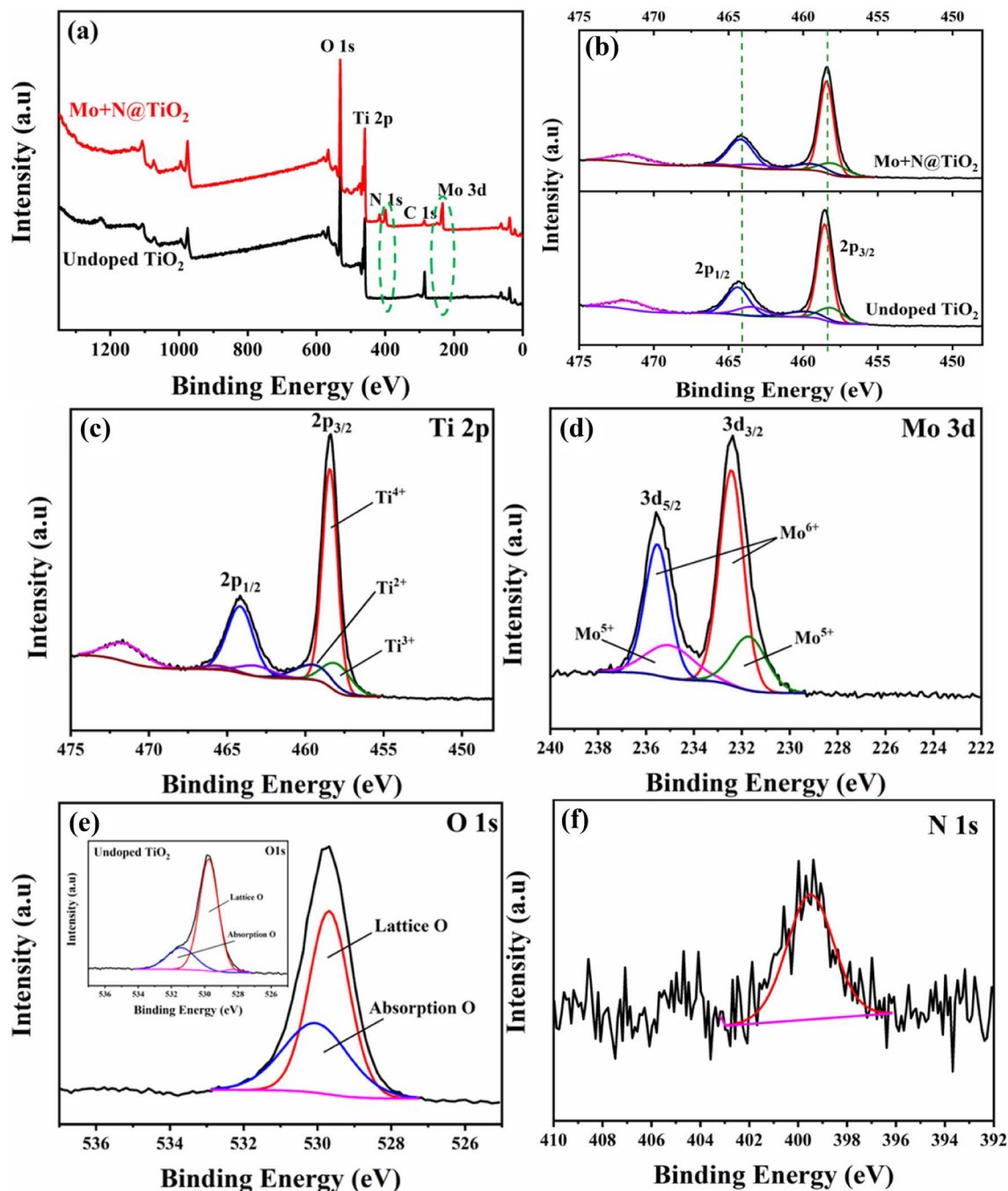
Fig. 4 (a) The XPS survey spectra and (b) Ti2p XPS spectra of undoped TiO_2 and the (Mo + N) codoped TiO_2 nanocomposite; the XPS spectra of the (c) Ti2p, (d) Mo3d, (e) O 1s, (f) N 1s core levels of the (Mo + N) codoped TiO_2 nanocomposite. The inset in Fig. 4(e) shows the O 1s spectrum of undoped TiO_2.

3.6. Photocatalytic activity of the synthesized photocatalysts

The photocatalytic activity of the as-prepared (Mo + N) codoped TiO_2 nanocomposite was evaluated based on the degradation of MO in an aqueous solution under UV-light irradiation. The change in MO concentration at λ_{max} (482 nm) was monitored using a UV-vis spectrophotometer. Aqueous suspensions of undoped and doped TiO_2 nanopowders were used for the UV-vis absorption studies. Fig. 6 shows the changes in the absorption spectra of MO in the presence of undoped TiO_2 and the (Mo + N) codoped TiO_2 nanocomposite. In the dark condition, there was no significant change in MO concentration; consequently, no significant change was detected in the adsorption of MO on the surface of the as-prepared catalysts . This indicates that the decolorization was primarily caused by the photocatalytic degradation of MO rather than its physiochemical adsorption on the surface of the nanostructured hybrid. Moreover, in the absence of a catalyst, <0.3% of MO was degraded after 30 min
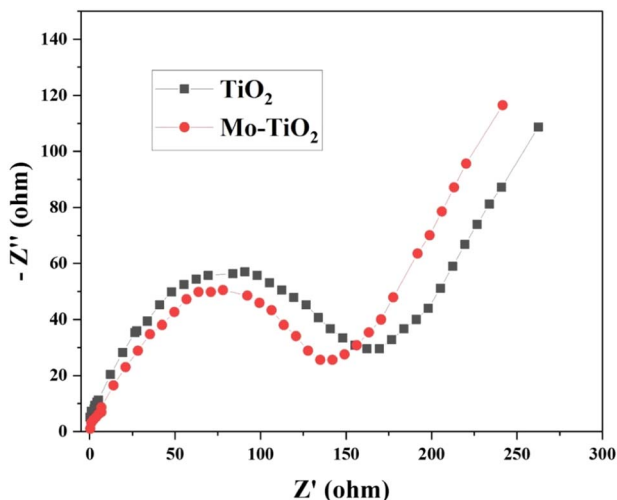
Fig. 5 The electrochemical impedance spectra (EIS) of the undoped TiO$_2$ and Mo–TiO$_2$ samples.

doping would generate energy states within the bandgap of TiO$_2$, which presumably shifts the optical absorption edge from the UV range to the visible light range. This consequently enhances light absorption and minimizes electron–hole recombination.[61,63] Moreover, N can easily substitute O in the TiO$_2$ lattice owing to its comparable atomic size with O. The small ionization energy and high stability of N lead to the construction of an energy level above the VB of TiO$_2$, which decreases the optical energy bandgap of TiO$_2$ and allows it to absorb light of higher wavelengths.[64,65] Furthermore, it acts as a trapping center for the photogenerated electrons and suppresses the recombination rate of the photogenerated electrons and holes.[64,65] This synergistic effect caused by the co-doping of metal and non-metal ions considerably enhances the photocatalytic activity of TiO$_2$.

Note that no additional peaks were observed in the UV-vis spectra, which indicates that the photodegradation of the tested dye occurs without the formation of hazardous organic intermediates.

The pH of the solution considerably influences the catalyst surface charge and plays an important role in the photocatalytic
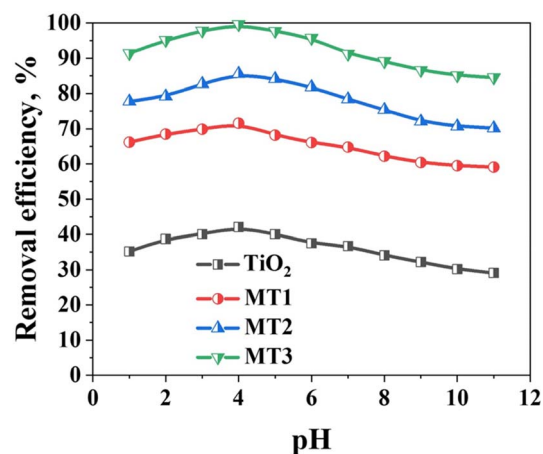
under UV irradiation, which demonstrates the high photostability of MO under UV light irradiation and that the auto-degradation of MO can be ignored, as shown in Fig. 6. After a few minutes of UV-irradiation, the addition of 10 mg of the fabricated photocatalysts to 10 mL of 50 mgL^{-1} MO leads to a significant decrease in absorption intensity owing to the decolorization of the dye. This reveals the improvement in the photocatalytic activity of the (Mo + N) codoped TiO$_2$ catalysts with increasing Mo content in the following sequence MT1 ‹ MT2 ‹ MT3. Furthermore, the photocatalytic activity of the TiO$_2$ catalyst was highly enhanced by Mo/N co-doping compared with undoped TiO$_2$. The improvement in TiO$_2$ photocatalytic performance is related to the changing physical properties of the nanoparticles with Mo and N doping, producing alterations in the crystal structure and energy bandgap, as well as elemental composition. The ionic radius of Mo^{6+} is 0.062 nm, which is almost identical to that of Ti^{4+} (0.068 nm); therefore the Mo^{6+} ions can substitute Ti^{4+} in the TiO$_2$ anatase crystal lattice, which would minimize lattice distortion.[22,61,62] Mo

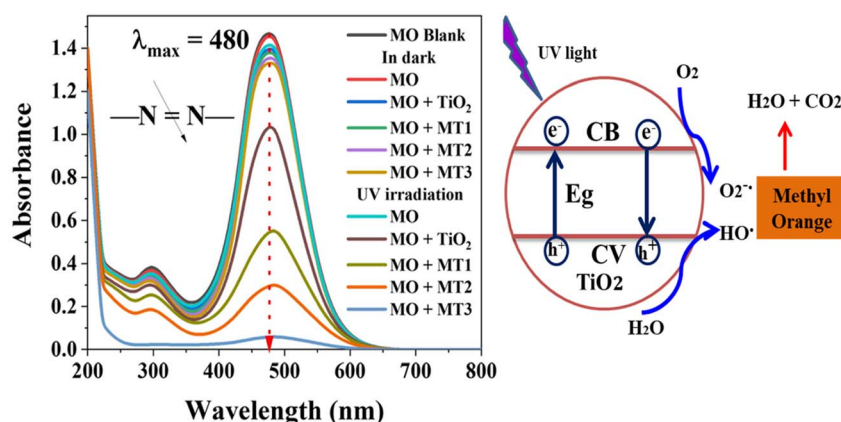Fig. 7 The effect of pH on the degradation of MO in the presence of TiO$_2$, MT1, MT2, and MT3 at the optimal condition.

Fig. 6 The absorption spectra of the MO dye during the degradation process catalyzed by the as-prepared nanocomposites at λ_{max} = 480 nm.

reaction, as well as the adsorption of the dye on the photocatalyst surface.[66,67] Fig. 7 shows the effect of solution pH (1 to 11) on MO degradation. A fixed weight (10 mg) of the as-synthesized photo-catalysts and a constant 10 mL volume of the 50 mgL^{-1} MO solution at room temperature were used in the experiment and irradiation for 30 minutes under a UV light. At pH = 4, MO was almost completely degraded (99.6%) within 30 min of the photoelectrocatalytic process. Moreover, the MO degradation efficiency apparently decreased with an increase in the pH value. The high MO removal efficiency under acidic conditions is related to the influence of the H$^+$ ions since they can be adsorbed on the surface of the photocatalyst, making it positively charged. The positively charged surface allows the UV-generated e$^-$ to migrate and interact with the adsorbed O$_2$ molecules, forming $\cdot$O$_2$. Furthermore, the positively charged surface might hinder the recombination of e$^-$ and h$^+$, additionally leading to OH$\cdot$ formation through the interaction of h$^+$ and H$_2$O.[66,67] Furthermore, at lower pH, the MO molecules exist in the quinonoid form, and the degradation rate may further increase in the absence of the stable azo bond.[66] Moreover, the surface of TiO$_2$ is positively charged under acidic conditions, triggering TiO$_2$ to adsorb more negatively charged organic dye

molecules on the surface and thus enhancing the photocatalytic efficiency.[66,67] However, in the alkaline condition, relatively lesser interactions would occur between the negatively charged TiO$_2$ and the organic dye anions, which decreases the amount of dye adsorbed on the surface and inhibits the photocatalytic process.[66,67]

Fig. 8 shows the degree of MO degradation by the as-prepared (Mo + N) TiO$_2$ catalysts with different Mo contents as a function of reaction time. Pure TiO$_2$ demonstrates a degradation rate of 42.1% after 30 min, and the molybdenum-doped materials exhibited improved photocatalytic performance than undoped TiO$_2$. The quantity of MO degraded by MT1, MT2, and MT3 within the first 5 min was 19.8, 31.6%, and 51.6%, respectively. Moreover, MT3 revealed the highest efficiency of 99.6% when the contact time was increased to 30 min, whereas the MT1 and MT2 photocatalysts showed degradation rates of 71.7% and 85.6%, respectively. Herein, higher concentrations of the dopant molybdenum led to higher degradation.

The reaction kinetics was investigated to understand the photocatalytic MO dye degradation behavior of the (Mo + N) codoped TiO$_2$ nanocomposite. To properly compare the breakdown rates, the MO content was normalized by its value at the onset of light irradiation (C_t/C_o) and plotted *versus* t, as shown in Fig. 9. The time zero on the horizontal axis of the plot denotes the commencement of light irradiation, at which the C_t/C_o value was set to 1 for all circumstances. The change in the MO adsorption peak value with time from 0 to 30 min in the presence of pure TiO$_2$, MT1, MT2, and MT3 was investigated with
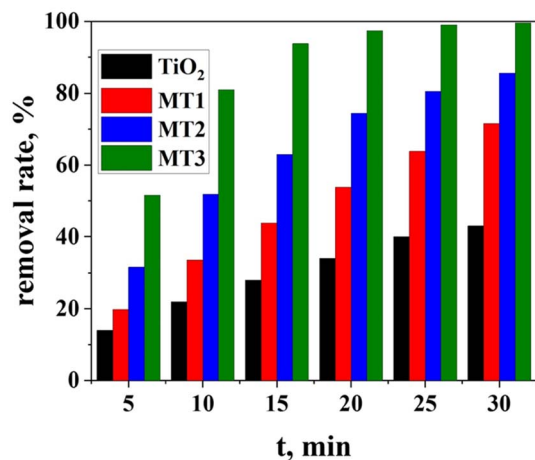

Fig. 8   The MO removal rates of the synthesized photocatalysts.

Table 1 The pseudo-first-order kinetic model of photocatalytic MO degradation by TiO$_2$, MT3, MT2, and MT1 at pH 4

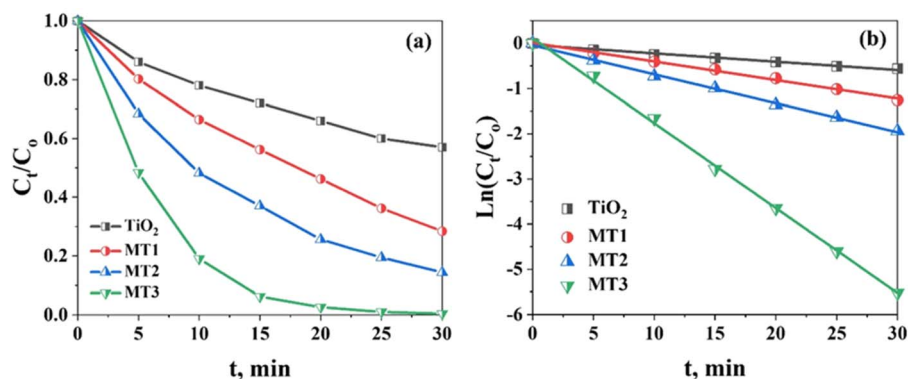| Photocatalyst	Pseudo-first-order kinetic parameter	
	K	R^2
TiO$_2$	1.83×10^{-2}	0.98116
MT1	4.09×10^{-2}	0.99536
MT2	6.405×10^{-2}	0.99728
MT3	1.87×10^{-1}	0.99892

Fig. 9   (a) The MO degradation efficiency of TiO$_2$, MT1, MT2 and MT3; (b) the pseudo-first-order kinetics of MO photodegradation using TiO$_2$, MT1, MT2, and MT3 as photocatalysts at pH = 4.
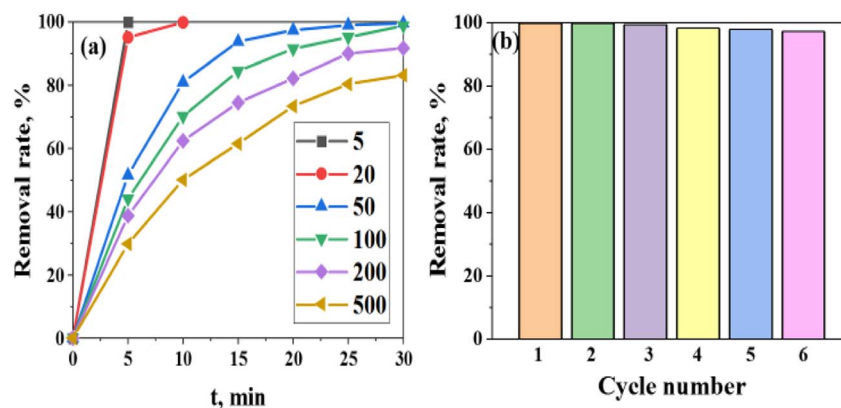
Fig. 10 (a) The degradation efficiency (%) of the (Mo + N)/TiO$_2$ photocatalyst as a function of the initial MO concentration at pH 4. (b) Reusability studies of the (Mo + N)/TiO$_2$ photocatalyst.

a starting MO concentration of 50 mgL^{-1} and pH 4 Fig. 9(a). The photocatalytic degradation of most organic pollutants at the liquid–solid interface can be expressed *via* a pseudo-first-order kinetic model equation $\ln(C/C_o) = -Kt$,[68] where C_0 represents the initial concentration of MO, C represents the concentration of MO at time t and k is the rate constant (min^{-1}).

The MO degradation data obtained using pure TiO$_2$, MT1, MT2, and MT3 was fitted to the pseudo-first-order model. The correlation constant of the fitted line was calculated to be $R^2 > 0.99$ for the doped TiO$_2$ samples (MT1, MT2, and MT3) and 0.981 for pure TiO$_2$, indicating that their photocatalytic degradation process matches the pseudo-first-order kinetic model. A sloped line was generated from the linear correlation between $\ln(C/C_o)$ and t, and it was used to get the values of k, as summarized in Table 1. The apparent reaction rate constant of MT3 was 1.87×10^{-1} min^{-1} at pH 4, while for undoped TiO$_2$, a lower reaction rate of 1.83×10^{-2} min^{-1} was detected, as shown in Fig. 9(b). Therefore, the catalyst (Mo + N) codoped TiO$_2$ nanocomposite possesses greater photocatalytic activity than pure TiO$_2$, and the color removal rate considerably increased when (Mo + N)-doped TiO$_2$ was used as the catalyst.

The effect of initial MO concentration on the photocatalytic behavior of (Mo + N)-doped TiO$_2$ is important to determine the efficiency of MO degradation.[69–71] The photocatalytic degradation of MO by (Mo + N)-doped TiO$_2$ at different initial MO concentrations was investigated under the optimal operating conditions of a single solution system (pH 4, contact time 30 min at 25 °C, 10 mg of the catalyst, and 10 mL of MO solution). Several MO concentrations of 5, 20, 50, 100, 200, and 500 mgL^{-1} were tested under UV light. The degradation efficiency was reduced as the initial concentration of MO was increased above 100 mgL^{-1}, reaching 83.2% in the case of 500 mgL^{-1} MO after 30 min of contact time, as shown in Fig. 10(a). Further, the adsorption of MO molecules on the surface of (Mo + N)-doped TiO$_2$ was realized by increasing the MO concentration. Several layers of adsorbed dye molecules are formed on the catalyst surface at an excessive dose, which inhibits the photoreaction because it hinders the direct contact of the light with the catalyst in order to generate hydroxyl radicals.[62,69–71]

Photocatalyst stability is one of the most important aspects for industrial processing and reversing the possibility of catalyst reuse.[62,69] It is considered one of the important indicators of the practical benefits and utility of a photocatalyst.[62,69] The stability of (Mo + N)-doped TiO$_2$ as a photocatalyst was examined after the fifth degradation run, as shown in Fig. 10(b). The degradation efficiency decreased from 99.6 to 97.11% after five runs, which demonstrates the higher degradation efficiency and stability of the (Mo + N)/TiO$_2$ photo-catalyst. The decrease in efficiency is strongly attributed to the loss of adsorption sites owing to the difficulty in removing the degradation by-products from the (Mo + N)/TiO$_2$ photocatalyst surface, such as sulfur-containing compounds. Therefore, the as-synthesized (Mo + N)-doped TiO$_2$ catalyst reveals excellent efficiency in the photodegradation of MO dye with minor efficiency loss and great durability.

The photocatalytic activity results obtained in this research were compared with the photocatalytic activity of other titanium dioxide/molybdenum photocatalysts. For example, Kanakaraju *et al.*[72] synthesized a series of titanium dioxide/molybdenum photocatalysts with different molybdenum concentrations (1–10 wt%) and demonstrated that the best-performing titanium dioxide/molybdenum (3 wt%) photocatalyst yielded a methyl orange photodegradation efficiency of 94.5% within 120 min of UV irradiation. Islam *et al.*[73] prepared an Ag/MoO$_3$/TiO$_2$ photocatalyst, and its maximum photodegradation efficiency was found to be 95.6% within 300 min of UV irradiation. These results demonstrate that the (Mo + N)-doped TiO$_2$ catalyst obtained in this research demonstrates better efficiency, as evidenced by its higher photocatalytic activity towards methyl orange (99.6% within 30 min of UV irradiation).

4. Conclusion

A simple one-step hydrothermal process followed by calcination treatment was used to prepare a Mo and N codoped TiO$_2$ nanocomposite with induced oxygen vacancies. The results reveal that the molybdenum and nitrogen atoms substitute the oxygen atoms in the TiO$_2$ crystal lattice. The as-prepared nanocomposites revealed excellent photocatalytic activity

toward methyl orange degradation under UV light illumination. The photocatalytic activity of the TiO_2 catalyst was considerably enhanced by the Mo/N co-doping. The photocatalytic activity of doped TiO_2 improved with increasing Mo content from MT1 to MT3. After 30 minu of contact time, the MT3 catalyst revealed the highest efficiency of 99.6%. The formation of Ti^{3+} and Mo^{5+}, which work collaboratively with the N dopant to generate oxygen vacancies, plays an important role in visible light absorption and enhancing photocatalytic activity.

Conflicts of interest

There are no conflicts to declare.

Acknowledgements

References

1 A. L. Linsebigler, G. Lu and J. T. Yates, Photocatalysis on TiO_2 Surfaces: Principles, Mechanisms, and Selected Results, *Chem. Rev.*, 1995, **95**, 735–758.

2 K. R. Reddy, M. Hassan and V. G. Gomes, Hybrid nanostructures based on titanium dioxide for enhanced photocatalysis, *Appl. Catal., A*, 2015, **489**, 1–16.

3 P. Cheng, Y. Wang, L. Xu, P. Sun, Z. Su, F. Jin, F. Liu, Y. Sun and G. Lu, High specific surface area urchin-like hierarchical ZnO-TiO_2 architectures: Hydrothermal synthesis and photocatalytic properties, *Mater. Lett.*, 2016, **175**, 52–55.

4 P. S. Basavarajappa, S. B. Patil, N. Ganganagappa, K. R. Reddy, A. V. Raghu and C. V. Reddy, Recent progress in metal-doped TiO_2, non-metal doped/codoped TiO_2 and TiO_2 nanostructured hybrids for enhanced photocatalysis, *Int. J. Hydrogen Energy*, 2020, **45**, 7764–7778.

5 F. Opoku, E. M. Kiarii and P. P. Govender, *Nanotechnology for Water and Wastewater Treatment Using Graphene Semiconductor Composite Materials*, 2020, vol. 32, pp. 1–34.

6 M. N. Chong, B. Jin, C. W. Chow and C. Saint, Recent developments in photocatalytic water treatment technology: a review, *Water Res.*, 2010, **44**, 2997–3027.

7 A. N. Banerjee, The design, fabrication, and photocatalytic utility of nanostructured semiconductors: focus on TiO_2-based nanostructures, *Nanotechnol., Sci. Appl.*, 2011, **4**, 35–65.

8 D. G. Rickerby, Nanostructured Titanium Dioxide for Photocatalytic Water Treatment, in *Nanomaterials for Environmental Protection* ed. B.I. Kharisov, O.V. Kharissova and H.V.R. Dias, 2014, ch. 10, pp. 169–182, DOI: **10.1002/9781118845530**.

9 C. Giuseppe, Z. Massimo, R. Francesco and G. Maria Grazia, TiO_2 Nanostructures and Nanocomposites for Sustainable Photocatalytic Water Purification, in *Green Nanotechnology*, ed. L. L. Marcelo and S. Sonia, IntechOpen, Rijeka, 2016, ch. 4, DOI: **10.5772/62620**.

10 D. H. Wang, L. Jia, X. L. Wu, L. Q. Lu and A. W. Xu, One-step hydrothermal synthesis of N-doped TiO_2/C nanocomposites with high visible light photocatalytic activity, *Nanoscale*, 2012, **4**, 576–584.

11 A. Khlyustova, N. Sirotkin, T. Kusova, A. Kraev, V. Titov and A. Agafonov, Doped TiO_2: the effect of doping elements on photocatalytic activity, *Mater. Adv.*, 2020, **1**, 1193–1201.

12 T. Khan, G. Bari, H.-J. Kang, T.-G. Lee, J.-W. Park, H. Hwang, S. Hossain, J. Mun, N. Suzuki, A. Fujishima, J.-H. Kim, H. Shon and Y.-S. Jun, Synthesis of N-Doped TiO_2 for Efficient Photocatalytic Degradation of Atmospheric NO_x, *Catalysts*, 2021, **11**, 109.

13 R. V. Nair, V. S. Gummaluri, M. V. Matham and C. Vijayan, A review on optical bandgap engineering in TiO_2 nanostructures via doping and intrinsic vacancy modulation towards visible light applications, *J. Phys. D: Appl. Phys.*, 2022, **55**, 313003.

14 V. Kumaravel, S. Rhatigan, S. Mathew, M. C. Michel, J. Bartlett, M. Nolan, S. J. Hinder, A. Gascó, C. Ruiz-Palomar, D. Hermosilla and S. C. Pillai, Mo doped TiO_2: impact on oxygen vacancies, anatase phase stability and photocatalytic activity, *JPhys Mater.*, 2020, **3**, 025008.

15 M. Zhang, B. Nian, Z. Wu, J. Guo, Z. Chen, C. Yuan, X. Huang, Y. Shen, H. Zhang and E. Tang, Molybdenum(V)-mediated switching of the C(sp(2))-Se bond of phenylselenyl-functionalized arenes or heterocycles under mild conditions, *Chem. Commun.*, 2023, **59**, 7599–7602.

16 Y. Zhang, W. Li, Z. Hu, X. Jing and L. Yu, Mo@PANI-catalyzed oxidative deoximation reaction, *Chin. Chem. Lett.*, 2024, **35**, 108938.

17 J. Zhang, J. Xi and Z. Ji, Mo + N Codoped TiO_2 sheets with dominant {001} facets for enhancing visible-light photocatalytic activity, *J. Mater. Chem.*, 2012, **22**, 17700.

18 M. Khan, J. Xu, N. Chen and W. Cao, First principle calculations of the electronic and optical properties of pure and (Mo, N) co-doped anatase TiO_2, *J. Alloys Compd.*, 2012, **513**, 539–545.

19 S. Wang, L. N. Bai, H. M. Sun, Q. Jiang and J. S. Lian, Structure and photocatalytic property of Mo-doped TiO_2 nanoparticles, *Powder Technol.*, 2013, **244**, 9–15.

20 M. L. Belikov and S. A. Safaryan, Adsorptive and Photocatalytic Properties of Molybdenum-Modified Titanium Dioxide, *Inorg. Mater.*, 2022, **58**, 715–722.

21 Y. H. Ahmad, A. S. Abu Hatab, A. T. Mohamed, M. S. Al-Kuwari, A. S. Aljaber and S. Y. Al-Qaradawi, Microwave-Assisted Solvothermal Synthesis of Mo-Doped TiO_2 with Exceptional Textural Properties and Superior Adsorption Kinetics, *Nanomaterials*, 2022, **12**, 2051.

22 N. Erdogan, J. Park and A. Ozturk, Synthesis and enhanced photocatalytic activity of molybdenum, iron, and nitrogen triple-doped titania nanopowders, *Ceram. Int.*, 2016, **42**, 16766–16774.

23 S. Esposito, N. Ditaranto, G. Dell'Agli, R. Nasi, P. Rivolo and B. Bonelli, Effective Inclusion of Sizable Amounts of Mo

within TiO₂ Nanoparticles Can Be Obtained by Reverse Micelle Sol-Gel Synthesis, *ACS Omega*, 2021, **6**, 5379–5388.

24 K. Tan, H. Zhang, C. Xie, H. Zheng, Y. Gu and W. F. Zhang, Visible-light absorption and photocatalytic activity in molybdenum- and nitrogen-codoped TiO₂, *Catal. Commun.*, 2010, **11**, 331–335.

25 S. Hu, F. Li and Z. Fan, Enhanced Visible Light Activity and Stability of TiO₂ Nanopowder by co-doped with Mo and N, *Bull. Korean Chem. Soc.*, 2012, **33**, 1269–1274.

26 S. Esposito, N. Ditaranto, G. Dell'Agli, R. Nasi, P. Rivolo and B. Bonelli, Effective Inclusion of Sizable Amounts of Mo within TiO₂ Nanoparticles Can Be Obtained by Reverse Micelle Sol–Gel Synthesis, *ACS Omega*, 2021, **6**, 5379–5388.

27 B. Houng, C. C. Liu and M. T. Hung, Structural, electrical and optical properties of molybdenum-doped TiO2 thin films, *Ceram. Int.*, 2013, **39**, 3669–3676.

28 J.-g. Huang, X.-t. Guo, B. Wang, L.-y. Li, M.-x. Zhao, L.-l. Dong, X.-j. Liu and Y.-t. Huang, Synthesis and Photocatalytic Activity of Mo-Doped TiO₂ Nanoparticles, *J. Spectrosc.*, 2015, **2015**, 681850.

29 L. Yin, Q. Zhou and X. Tang, The Mechanism of Nanocrystalline TiO₂ Derived by Sol-Gel Process, *Funct. Mater.*, 1999, **30**, 407–409.

30 R. Das and S. Sarkar, X-ray diffraction analysis of synthesized silver nanohexagon for the study of their mechanical properties, *Mater. Chem. Phys.*, 2015, **167**, 97–102.

31 S.-Y. Luo, B.-X. Yan and J. Shen, Enhancement of photoelectric and photocatalytic activities: Mo doped TiO₂ thin films deposited by sputtering, *Thin Solid Films*, 2012, **522**, 361–365.

32 L. Alexander and H. P. Klug, Basic Aspects of X-Ray Absorption in Quantitative Diffraction Analysis of Powder Mixtures, *Anal. Chem.*, 2002, **20**, 886–889.

33 R. López and R. Gómez, Photocatalytic Degradation of 4-Nitrophenol on Well Characterized Sol–Gel Molybdenum Doped Titania Semiconductors, *Top. Catal.*, 2011, **54**, 504–511.

34 A. Monshi, M. R. Foroughi and M. R. Monshi, Modified Scherrer Equation to Estimate More Accurately Nano-Crystallite Size Using XRD, *World J. Nano Sci. Eng.*, 2012, **02**, 154–160.

35 A. T. Kuvarega, PhD thesis, University of Johannesburg, South Africa, 2012.

36 K. S. W. Sing, Reporting physisorption data for gas/solid systems with special reference to the determination of surface area and porosity (Recommendations 1984), *Pure Appl. Chem.*, 1985, **57**, 603–619.

37 S. Yurdakal, C. Garlisi, L. Özcan, M. Bellardita and G. Palmisano, Chapter 4 - (Photo)catalyst Characterization Techniques: Adsorption Isotherms and BET, SEM, FTIR, UV–Vis, Photoluminescence, and Electrochemical Characterizations, in *Heterogeneous Photocatalysis*, ed. G. Marcì and L. Palmisano, Elsevier, 2019, pp. 87–152, DOI: **10.1016/B978-0-444-64015-4.00004-3**.

38 Y. J. Choi, Z. Seeley, A. Bandyopadhyay, S. Bose and S. A. Akbar, Aluminum-doped TiO₂ nano-powders for gas sensors, *Sens. Actuators, B*, 2007, **124**, 111–117.

39 G. He, J. Zhang, Y. Hu, Z. Bai and C. Wei, Dual-template synthesis of mesoporous TiO₂ nanotubes with structure-enhanced functional photocatalytic performance, *Appl. Catal., B*, 2019, **250**, 301–312.

40 Y. Jiang, W.-F. Chen, P. Koshy and C. C. Sorrell, Enhanced photocatalytic performance of nanostructured TiO₂ thin films through combined effects of polymer conjugation and Mo-doping, *J. Mater. Sci.*, 2019, **54**, 5266–5279.

41 J.-g. Huang, X.-t. Guo, B. Wang, L.-y. Li, M.-x. Zhao, L.-l. Dong, X.-j. Liu and Y.-t. Huang, Synthesis and Photocatalytic Activity of Mo-Doped TiO2Nanoparticles, *J. Spectrosc.*, 2015, **2015**, 1–8.

42 S. Zhu, Y. Dong, X. Xia, X. Liu and H. Li, Synthesis of Mo-doped TiO₂ nanowires/reduced graphene oxide composites with enhanced photodegradation performance under visible light irradiation, *RSC Adv.*, 2016, **6**, 23809–23815.

43 M. P. Blanco-Vega, J. L. Guzmán-Mar, M. Villanueva-Rodríguez, L. Maya-Treviño, L. L. Garza-Tovar, A. Hernández-Ramírez and L. Hinojosa-Reyes, Photocatalytic elimination of bisphenol A under visible light using Ni-doped TiO 2 synthesized by microwave assisted sol-gel method, *Mater. Sci. Semicond. Process.*, 2017, **71**, 275–282.

44 H. M. Yadav, S. V. Otari, R. A. Bohara, S. S. Mali, S. H. Pawar and S. D. Delekar, Synthesis and visible light photocatalytic antibacterial activity of nickel-doped TiO₂ nanoparticles against Gram-positive and Gram-negative bacteria, *J. Photochem. Photobiol., A*, 2014, **294**, 130–136.

45 L.-L. Lai, W. Wen and J.-M. Wu, Ni-doped rutile TiO₂ nanoflowers: low-temperature solution synthesis and enhanced photocatalytic efficiency, *RSC Adv.*, 2016, **6**, 25511–25518.

46 J.-Q. Bai, W. Wen and J.-M. Wu, Facile synthesis of Ni-doped TiO₂ ultrathin nanobelt arrays with enhanced photocatalytic performance, *CrystEngComm*, 2016, **18**, 1847–1853.

47 I. G. Alhindawy, H. I. Mira, A. O. Youssef, S. M. Abdelwahab, A. A. Zaher, W. A. El-Said, E. A. Elshehy and A. M. Abdelkader, Cobalt doped titania-carbon nanosheets with induced oxygen vacancies for photocatalytic degradation of uranium complexes in radioactive wastes, *Nanoscale Adv.*, 2022, **4**, 5330–5342.

48 I. G. Alhindawy, E. A. Elshehy, A. O. Youssef, S. M. Abdelwahab, A. A. Zaher, W. A. El-Said, H. I. Mira and A. M. Abdelkader, Improving the photocatalytic performance of cobalt-doped titania nanosheets by induced oxygen vacancies for efficient degradation of organic pollutants, *Nano-Struct. Nano-Objects*, 2022, 31.

49 H. Khan and D. Berk, Characterization and mechanistic study of Mo⁺⁶ and V⁺⁵ codoped TiO₂ as a photocatalyst, *J. Photochem. Photobiol., A*, 2014, **294**, 96–109.

50 F. Feng, W. Yang, S. Gao, C. Sun and Q. Li, Postillumination Activity in a Single-Phase Photocatalyst of Mo-Doped TiO₂ Nanotube Array from Its Photocatalytic "Memory", *ACS Sustain. Chem. Eng.*, 2018, **6**, 6166–6174.

51 D. Mardare, N. Cornei, D. Luca, M. Dobromir, Ş. A. Irimiciuc, L. Pungă, A. Pui and C. Adomniţei, Synthesis and

hydrophilic properties of Mo doped TiO2 thin films, *J. Appl. Phys.*, 2014, 115.

52 D. Xue, J. Luo, Z. Li, Y. Yin and J. Shen, Enhanced Photoelectrochemical Properties from Mo-Doped TiO$_2$ Nanotube Arrays Film, *Coatings*, 2020, **10**, 75.

53 O. Avilés-García, J. Espino-Valencia, R. Romero, J. L. Rico-Cerda, M. Arroyo-Albiter and R. Natividad, W and Mo doped TiO$_2$: Synthesis, characterization and photocatalytic activity, *Fuel*, 2017, **198**, 31–41.

54 G. Wu, J. Wen, S. Nigro and A. Chen, One-step synthesis of N- and F-codoped mesoporous TiO2 photocatalysts with high visible light activity, *Nanotechnology*, 2010, **21**, 85701.

55 X. Cheng, X. Yu, Z. Xing and J. Wan, Enhanced Photocatalytic Activity of Nitrogen Doped TiO$_2$ Anatase Nano-Particle under Simulated Sunlight Irradiation, *Energy Procedia*, 2012, **16**, 598–605.

56 L. Bergamonti, G. Predieri, Y. Paz, L. Fornasini, P. P. Lottici and F. Bondioli, Enhanced self-cleaning properties of N-doped TiO$_2$ coating for Cultural Heritage, *Microchem. J.*, 2017, **133**, 1–12.

57 M. Xing, J. Zhang and F. Chen, New approaches to prepare nitrogen-doped TiO$_2$ photocatalysts and study on their photocatalytic activities in visible light, *Appl. Catal., B*, 2009, **89**, 563–569.

58 J. Wang, N. Tafen de, J. P. Lewis, Z. Hong, A. Manivannan, M. Zhi, M. Li and N. Wu, Origin of photocatalytic activity of nitrogen-doped TiO2 nanobelts, *J. Am. Chem. Soc.*, 2009, **131**, 12290–12297.

59 I. G. Alhindawy, E. A. Elshehy, A. O. Youssef, S. M. Abdelwahab, A. A. Zaher, W. A. El-Said, H. I. Mira and A. M. Abdelkader, Improving the photocatalytic performance of cobalt-doped titania nanosheets by induced oxygen vacancies for efficient degradation of organic pollutants, *Nano-Struct. Nano-Objects*, 2022, **31**, 100888.

60 E. A. Elshehy, Removal of uranium ions from liquid radioactive waste using modified aluminosilica, *Sep. Sci. Technol.*, 2017, **52**, 1852–1861.

61 M. Khan, J. Xu, W. Cao and Z. K. Liu, Mo-doped TiO$_2$ with enhanced visible light photocatalytic activity: a combined experimental and theoretical study, *J. Nanosci. Nanotechnol.*, 2014, **14**, 6865–6871.

62 T. Zhang, B. Yu, D. Wang and F. Zhou, Molybdenum-doped and anatase/rutile mixed-phase TiO$_2$ nanotube photoelectrode for high photoelectrochemical performance, *J. Power Sources*, 2015, **281**, 411–416.

63 J. Zhou, B. Feng, X. Lu and K. Duan, Novel one-step fabrication of highly ordered Mo-doped TiO$_2$ nanotubes

arrays with enhanced visible light catalytic activity, *J. Mater. Sci.: Mater. Electron.*, 2018, **29**, 18388–18396.

64 S. A. Ansari, M. M. Khan, M. O. Ansari and M. H. Cho, Nitrogen-doped titanium dioxide (N-doped TiO$_2$) for visible light photocatalysis, *New J. Chem.*, 2016, **40**, 3000–3009.

65 R. Li, T. Li and Q. Zhou, Impact of Titanium Dioxide (TiO$_2$) Modification on Its Application to Pollution Treatment—A Review, *Catalysts*, 2020, **10**, 804.

66 H. Zhu, R. Jiang, Y. Fu, Y. Guan, J. Yao, L. Xiao and G. Zeng, Effective photocatalytic decolorization of methyl orange utilizing TiO$_2$/ZnO/chitosan nanocomposite films under simulated solar irradiation, *Desalination*, 2012, **286**, 41–48.

67 S. Abbasi, M. Hasanpour, F. Ahmadpoor, M. Sillanpää, D. Dastan and A. Achour, Application of the statistical analysis methodology for photodegradation of methyl orange using a new nanocomposite containing modified TiO$_2$ semiconductor with SnO$_2$, *Int. J. Environ. Anal. Chem.*, 2019, **101**, 208–224.

68 Y. Ding, C. Yang, L. Zhu and J. Zhang, Photoelectrochemical activity of liquid phase deposited TiO$_2$ film for degradation of benzotriazole, *J. Hazard. Mater.*, 2010, **175**, 96–103.

69 M. S. Khan, C. F. Kait and M. I. A. Mutalib, *Photooxidative desulfurization for diesel using Fe/N−TiO$_2$ photocatalyst*, 2014, vol. 1621, pp. 10–16.

70 M. S. Khan, J. A. Shah, M. Arshad, S. A. Halim, A. Khan, A. J. Shaikh, N. Riaz, A. J. Khan, M. Arfan, M. Shahid, A. Pervez, A. A. Harasi and M. Bilal, Photocatalytic Decolorization and Biocidal Applications of Nonmetal Doped TiO$_2$: Isotherm, Kinetic Modeling and In Silico Molecular Docking Studies, *Molecules*, 2020, **25**, 4468.

71 M. S. Khan, J. A. Shah, N. Riaz, T. A. Butt, T. A. Butt, A. J. Khan, W. Khalifa, H. H. Gasmi, E. R. Latifee, M. Arshad, A. A. A. Al-Naghi, A. Ul-Hamid, M. Arshad and M. Bilal, Synthesis and Characterization of Fe-TiO$_2$ Nanomaterial: Performance Evaluation for RB5 Decolorization and In Vitro Antibacterial Studies, *Nanomaterials*, 2021, **11**, 436.

72 D. Kanakaraju, M. A. A. Jasni and Y. C. Lim, A highly photoresponsive and efficient molybdenum-modified titanium dioxide photocatalyst for the degradation of methyl orange, *Int. J. Environ. Sci. Technol.*, 2021, **19**, 5579–5594.

73 S. Kader, M. R. Al-Mamun, M. B. K. Suhan, S. B. Shuchi and M. S. Islam, Enhanced photodegradation of methyl orange dye under UV irradiation using MoO$_3$ and Ag doped TiO$_2$ photocatalysts, *Environ. Technol. Innovation*, 2022, **27**, 102476.